The role of tortuosity in filtration efficiency: a general network model for filtration

I. M. Griffiths[a,∗], I. Mitevski[b], I. Vujkovac[c], M. R. Illingworth[c], P. S. Stewart[d]

[a]*Mathematical Institute, University of Oxford, Radcliffe Observatory Quarter, Oxford OX2 6GG, United Kingdom*
[b]*Department of Applied Physics and Applied Mathematics, Columbia University, New York, NY, 10027*
[c]*New Jersey Institute of Technology, Newark, New Jersey 07102, USA*
[d]*School of Mathematics and Statistics, University of Glasgow, G12 8QW, UK*

Abstract

Filters are composed of a complex network of interconnected pores each with tortuous paths. We present a general network model to describe a filter structure comprising a random network of interconnected pores, relaxing traditional assumptions made with simplified theoretical models. We use the model to examine the dependence of the filter performance on both its underlying pore structure (expressed through the pore interconnectivity and porosity gradient) and the feed composition (expressed through the size of the contaminants). We find that a simple scaling allows the performance curves over a wide range of the filter material properties to be mapped onto a single master curve. We also study the link between the tortuosity of a filter and its resulting performance, leading to further self-similarity observations. When we vary the properties of the feed, however, the performance curves are distinct from one another and do not collapse onto a single master curve.

Our network model allows us to probe the behaviour of a complex and realistic filter configuration within a framework that is easy to implement and study, enabling accelerated testing and reducing experimental costs in filtration challenges.

Keywords: Filtration, Tortuosity, Network model, Mathematical modelling, Self-similarity

1. Introduction

Modelling particle filtration through a porous structure poses a significant challenge due to the random arrangement and interconnectivity of pores. Theoretical models for filters traditionally make a series of simplifying assumptions that enable a tractable set-up to be constructed and studied. For instance, this might be periodicity in the filter construct [1], or a lack of branching of pores [2, 3]. Such assumptions provide appropriate models for certain filters, for example track-etched membranes, which comprise approximately uniformly sized straight-through pores. However, in the majority of filters, pores are assorted in length, orientation and size, and form complex branching patterns. While idealistic mathematical frameworks retain the physics needed to provide much needed explanations for certain observed behaviour in filter operation (see, for example [1, 2], where the nature of the flux decline with time

is uncovered), it is natural to ask what additional insight can be gained by studying a more realistic filter set-up.

A step in this direction is taken in [4], for filters composed of a series of obstacles onto which material adheres. A 'pseudo-randomness' is introduced by considering a random arrangement within a suitably large representative volume and repeating this in space. This enables a study of the role of randomness to be conducted in the case of fibrous-type filters while retaining the elements of mathematical simplicity afforded by enforcing periodicity in the system. The authors use homogenization theory to derive upscaled models in which a cell problem comprising flow through a small number of randomly arranged obstacles needs to be solved only once. Some metrics, such as particle diffusivity are found to be largely unaffected by the relaxation of a periodic domain, while others, such as removal efficiency, are shown to be dependent on the underpinning structure. The results demonstrate that, while there is no universal best filter for a given task, depending on filtration requirements, either a periodic or a random filter

may offer superior performance.

In [1] and [3] first steps are taken towards probing the effect of pore branching, via continuum and discrete frameworks respectively. In both cases the physical set-up possesses an underlying periodic structure to facilitate the mathematical analysis.

In this paper we construct a fully general framework for filters comprising pores of arbitrary length and orientation that branch in a general manner. The filters are constructed by prescribing the number and location of exposed pores on the upper and lower surfaces and the junctions in the internal filter structure. The pores are connected according to prescribed guidelines on the maximum pore length. The flexibility in the derived network model allows us to probe the effect of pore structure in a way that models for idealistic filter geometries cannot.

We centre our study on the effect of tortuosity, one of the properties that is most easily lost in many of the idealized set-ups. In a real filter, as particles block pores, subsequent particles will take paths that become increasingly convoluted. When operating at a fixed pressure differential, this effect leads to an undesirable drop in the flux of processed fluid. On the other hand, the longer paths that particles must take through the filter leads to an increase in the chance that a particle is trapped. This improves the likelihood of a particle being removed by the filter rather than passing through uncaptured.

We assess the filter performance by considering how both the flux and the particle removal efficiency (fraction of particles removed) vary with total volume of fluid processed (the throughput), and study the connection between these two metrics and the tortuosity of the filter. Recognizing that in practice one wishes to maximize both the flux and the particle removal efficiency, we consider the product of these two quantities as a performance metric. In all cases, our performance metric falls with time, implying that the performance of a filter degrades with time. We generalize our metric to allow for scenarios in which different levels of importance are placed on the flux and particle removal efficiency.

We study the difference in performance of a given filter when filtering a feed composed of particles of different sizes, and the performance of filters with different pore interconnectivity for a given feed type.

We also use our model to study the effect of porosity gradients in a filter. Filters whose porosity decreases with penetration depth have been observed to improve efficiency and as a result have received attention [5, 6, 7, 8, 9]. The porosity gradient is chosen to balance the simultaneous reduction of contaminant concentration with depth that arises due to prior filtering. Such a set-up has been considered in the context of a filter comprising a series of obstacles through which contaminants must traverse (for example, a fibrous filter) [10, 11]. Here, homogenization theory is generalized to incorporate weak deviations from a periodic domain. The authors confirm the improved removal efficiency of porosity-graded filters and determine the optimal porosity gradient that removes the most contaminant before blocking.

Here, we consider the network analogue of such a porosity-graded filter, where the arrangement of pores is biased in the filter medium. Furthermore, our model filter is also able to exhibit a porosity gradient even when the porosity of the internal pore structure is uniform on average, by instead including a different density of upper and lower pores. This type of porosity gradient is observed in composite membranes [12], but is less well studied.

The results of the fully general pore-based network model derived in this paper are compared with those obtained for obstacle-laden filters considered in [4, 10, 11] where sensible, while areas in which this model is superior are probed, to add to the current understanding of the filtration process afforded by current theoretical models.

2. Model set-up

2.1. Filter construction

We consider a filter composed of a series of pores, represented as cylindrical pipes. For illustrative purposes we assume these to be of uniform radius in this paper but note that variability in pore radii is easily incorporated. Without loss of generality we can set the initial pore radius to unity; all subsequent distances are then measured relative to the pore radius. We consider a filter occupying the space $0 \leq x \leq L$, $0 \leq y \leq L$, $0 \leq z \leq H$ where the planes $z = 0$, H define the top and bottom surfaces of the filter respectively (see figure 1). In all of the results presented here we choose $L = H = 100$. We describe the filter pore structure through the number of pores N_{top} exposed on the top surface ($z = 0$) and the number of pores N_{bottom} exposed on the bottom surface ($z = H$). The interior pore structure ($0 < z < H$) is constructed by assigning a number, N_{int}, of points in the 3D interior space, which form the pore junctions. The location of the top and bottom pores and junctions are all set randomly. To construct the filter, each top-surface pore orifice is connected to all junctions beneath that lie within a certain distance, d, which
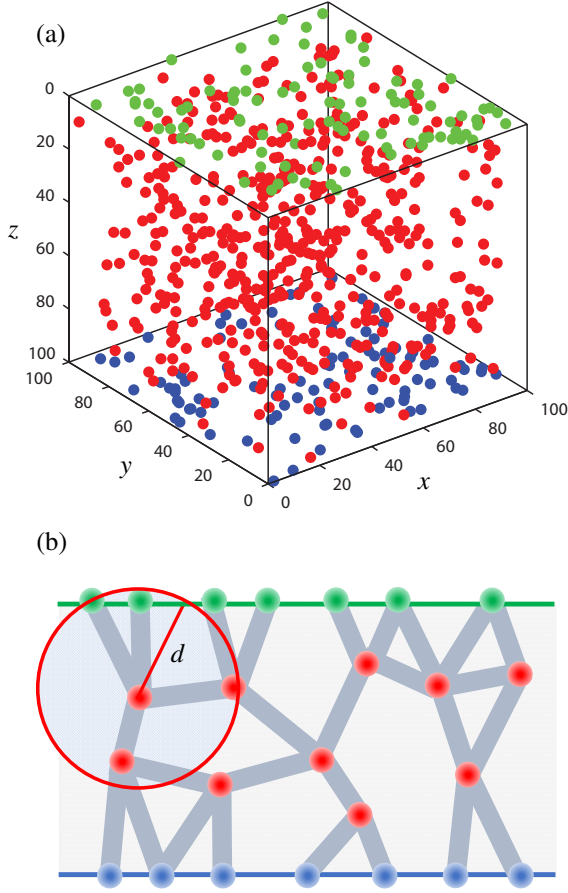
(a)

(b)

Figure 1: (a) 3D pore distribution within a filter, biased towards the top. Here, the filter is defined by $0 \leq x \leq L$, $0 \leq y \leq L$, $0 \leq z \leq H$, where the planes $z = 0$, H define the top and bottom surfaces of the filter respectively, with $L = H = 100$. The filter possesses $N_{\text{top}} = 100$ surface pores (green dots on $z = 0$), $N_{\text{bottom}} = 100$ exit pores (blue dots on $z = H$) and $N_{\text{int}} = 500$ internal pore junctions (red dots). (b) 2D schematic slice through a cross-section of the filter illustrating the pore network structure and interconnectivity distance d.

we denote as the *interconnectivity distance*. Similarly, internal pore junctions are connected to all surrounding junctions that lie within a distance d. This process continues until junctions are connected to the bottom-surface pores (see figure 1b). Given the random nature of distributing the junctions, in some cases surface-pore orifices may not connect to any junctions, internal junctions may not connect to any junctions, or outlet-pores may not connect to any junctions. In this case these pores or junctions are redundant.

The interior points are randomly but not necessarily uniformly distributed: we allow the filter structures to

possess a biased porosity distribution in the z direction.

We sample the z-locations of the interior points from a triangular distribution with probability density function

$$f(z) = \frac{1}{H}\left(1 + \alpha\left(z - \tfrac{1}{2}H\right)\right), \qquad 0 < z < H, \qquad (1)$$

where α is a parameter which sets the gradient of the distribution. Note that we require $-2/H \leq \alpha \leq 2/H$ to ensure that $f \geq 0$ for all z. Note also that the distribution is biased towards $z = H$ when $\alpha > 0$ and biased towards $z = 0$ when $\alpha < 0$.

Our procedure for computing the z-location of each point is as follows: for a point with z-location Z we sample the probability that $z \leq Z$ (for $0 \leq z \leq H$) as a random number from a uniform distribution between 0 and 1, denoted ξ. Hence,

$$P(z \leq Z) = \int_0^Z f \, \mathrm{d}z = \xi. \qquad (2)$$

For our particular choice of probability density function, (1), this integral can be evaluated analytically. This gives rise to a quadratic equation for Z with one root that lies in $0 \leq Z \leq H$ which provides an explicit formula for Z as a function of ξ.

This bias in the z-locations of the interior points means that the overall porosity of the filter will also be biased in the same way, as more pore connections will form in regions where these interior points are clustered. However, it is not possible to control the porosity distribution of the filter directly using this approach.

2.2. Filter operation

In all cases we consider the behaviour of the filter under constant applied transmembrane pressure difference ΔP. The flux q of a fluid with viscosity μ through a single cylindrical pore within the filter of length h, radius r, and pressure difference Δp across its length is given by Poiseuille's law [13]

$$q = \frac{\pi \Delta p \, r^4}{8\mu h}. \qquad (3)$$

As particles adhere to the pore walls, the pore radii and driving pressure must evolve in time, and so will the flux through the pores. Denoting the flux through the surface pores by q_i, where $1 \leq i \leq N_{\text{top}}$, the total flux through the filter is given by

$$Q = \sum_{i=1}^{N_{\text{top}}} q_i. \qquad (4)$$

3

We define the throughput, V, of the filter to be the total fluid processed up to a given time, t,

$$V = \int_0^t Q(s)\,\mathrm{d}s. \qquad (5)$$

Without loss of generality, we assume that one particle is contained in each unit of fluid. In this case, the throughput is then also conveniently equal to the number of particles that have entered the filter.

The flux through each pore in the filter structure is calculated using (3). The fluid pressure on the upper and lower surface orifices follows from the boundary conditions that enforce the constant transmembrane pressure difference, ΔP. However, the pressure at each internal junction must be calculated by imposing that the total flux into the junction must balance the total flux out in an analogous fashion to Kirchoff's law for electrical circuits.

2.3. Particle deposition

We consider a feed of particles with uniform concentration, and assume that each unit of fluid contains one particle. In this case, the throughput is also identified as the total number of particles that have entered the filter (which may or may not be captured).

As a particle arrives at the filter, the probability p_i of that particle entering a given surface pore, i, is defined as the ratio of the flux through that pore to the total flux through the filter:

$$p_i = \frac{q_i}{Q}. \qquad (6)$$

We consider a monodisperse feed composed of particles of radius a (relative to the initial pore radius). If $a > 1$ then the particles cannot enter the pores and are filtered out on the surface; if $a < 1$ the particles are able to enter into the pores. In our case we are interested in the internal behaviour of the filter, and so focus our attention on particle feeds with $a < 1$. We denote p_a as the probability of a particle adhering to the pore walls per unit length, and assume that this is a constant. The probability of adhering to the walls of a pore of length ℓ is then given by

$$p_\ell = 1 - (1 - p_a)^\ell. \qquad (7)$$

In all of the simulations reported below we choose $p_a = 0.01$. Other, more complex, adhesion laws could be applied, for example, by assuming the probability of adhesion within a pore is proportional to the transit time in that pore. Our model would readily generalize to cater for such scenarios, but here we choose the simpler form for illustrative clarity.

If a particle of radius a adheres to a pore of radius r and height h then we assume that the radius of that pore is modified to $\sqrt{r^2 - 4a^3/3h}$. This assumes that the particle's volume is distributed uniformly over the inner surface of that pore, which provides a good approximation, on average, for the pore constriction process due to particle deposition. If the particle does not adhere to the wall it passes through the pore until it reaches the junction. Once a particle reaches a junction, the subsequent pore that it enters is decided based on the local fluxes out of that junction in the probabilistic manner given by (6). The particle cannot enter pores where the flow is towards the junction. If a particle selects a pore to enter whose radius is smaller than the particle then the particle may not enter the pore and instead the pore entrance will block. In this case we assume that the pore blocks completely and no subsequent fluid may pass through this pore. If a particle makes its way to the bottom layer ($z = H$) without adhering to any pore wall it will escape.

The specific flow behaviour within any junction will be complex. However, this will not affect the ultimate destination of the particles that we capture in our model – at worst, the particles may experience a delay to their journey through the filter while transiting the junctions – so we do not model the specific junction flow here.

When the particle sticks, the flux through each pore is recalculated using the same procedure as before. The entire process of particle arrival, propagation through the filter, and recalculation of the pressure, flux, and radii is repeated until the total flux reaches zero and the filter is completely blocked.

In all of the calculations performed in this paper we are concerned with fluxes through the filter scaled relative to the initial flux. In doing so, the pressure difference ΔP and μ do not feature in the problem.

All graphs generated below are averaged over 100 simulations, with each simulation using a newly generated filter configuration with the same parameters that characterize the filter. This ensures that stochastic variations are suitably smoothed.

3. Quantifying the fouling process

To characterize our filter we introduce the notion of *interconnectivity*, *tortuosity* and *particle removal efficiency*.

We define the interconnectivity of the filter,

$$d = \frac{\text{maximum pore length in filter}}{\text{initial pore radius}}. \qquad (8)$$

We define the tortuosity, τ, as

$$\tau(V) = \frac{\text{average distance travelled by escaping particles}}{\text{filter thickness, } H}.$$
(9)

The average distance travelled by escaping particles at throughput V is determined by considering the previous N_τ particles that have entered the filter and calculating the average tortuosity of those particles that have escaped the filter, so that $\tau(V)$ is a moving average in V taken over the interval $[V - N_\tau, V + N_\tau]$, where we recall that the throughput V also corresponds to the total number of particles that have entered the filter with our definition of the particle concentration. In all of the simulations conducted in this paper, we consider $N_\tau = 500$. Note that this means that whenever we consider the evolution in terms of the throughput we present graphical results that begin at $V = 500$.

We define the particle removal efficiency as

$$E(V) = 1 - \text{fraction of particles that are unfiltered}.$$
(10)

The fraction of unfiltered particles at a given throughput V is defined as the total number of particles that escape the filter (out of the N_E particles that are inserted into the filter before that time), divided by N_E. As for the tortuosity, $E(V)$ is a moving average taken over the interval $[V - N_E, V + N_E]$. In all of the simulations considered in this paper we take $N_E = 500$.

In the following sections, we analyse the filter performance by considering the variation in the flux Q, particle removal efficiency E and tortuosity τ as the filtration process progresses. We make comparisons between the 3D model and the periodic filter arrangement considered in [1, 2] as well as exploring the additional predictions that this model can make, most notably, the effect of tortuosity.

We begin in §4 by assessing the relationship between tortuosity, porosity distribution and interconnectivity distance that emerges from the network construction we have chosen. In §5 we show how we may use our membrane characterization to extract other physical membrane properties. We then move on to consider the filtration performance. First we analyse the dependence of the performance on the material properties of the filter used, quantified through the interconnectivity distance, d, in §6, and the bias in porosity in §7, implemented either through the internal porosity gradient, α, or through a difference between the number of top and bottom surface pores, N_{top} and N_{bottom}. We then explore the performance of the filter when subjected to different

feed types, characterized through the contaminant particle size, in §8. Finally, in §9 we draw conclusions on the implications of our results and the potential application of the framework for the filtration industry.

4. Tortuosity relationship

There is a complex link between the tortuosity of a membrane and its porosity, pore interconnectivity and pore distribution. Relations have been proposed based on phenomenological laws and the results of numerical simulations in porous media, which link the tortuosity to porosity. The simplest of these stems from the Carman–Kozeny law, based on a simple capillary model for a porous medium, which predicts a relationship of the form $\tau = \phi^{3/2}$ where ϕ is the porosity [14]. We can extract a relationship for our more complex random porous network between the tortuosity τ and: the interconnectivity distance d; concentration of internal pore junctions, N_{int} (which is a measure of the porosity through equation (2)); concentration of the surface pores, N_{top} and N_{bottom}; and the porosity bias. Naively, one might anticipate that the tortuosity associated with a filter would decrease with increasing filter interconnectivity, as more direct routes become available. In our case, however, while the tortuosity does indeed decrease with increasing interconnectivity distance d for low values of d, we find that as d increases further the tortuosity rises again (figure 2a, blue curve).

We can gain insight into the non-monotonic dependence of tortuosity on d by comparing our model with that of a deterministic process, whereby particles *always* choose to enter the pore with the greatest flux. While this model is not expected to portray an accurate representation of real filter behaviour, it is instructive to consider, as in this case we find that the tortuosity does indeed monotonically decrease with increasing connectivity, tending towards 1, indicating that a straight path is taken as the interconnectivity distance becomes large (figure 2a, red curve).

This allows us to conclude that the non-monotonic dependence of tortuosity on interconnectivity distance is a direct result of the stochasticity of the system. Specifically, in our model, upon arrival at a junction, a particle chooses the next pore to enter with a *bias* towards those with larger flux but does not always choose the pore with the highest flux. As the number of junctions increases, the difference between the fluxes through each pore becomes less prominent. This has the combined result that the probability of a particle taking a route that is *not* the most direct increases as the number of possible paths that are available increases.
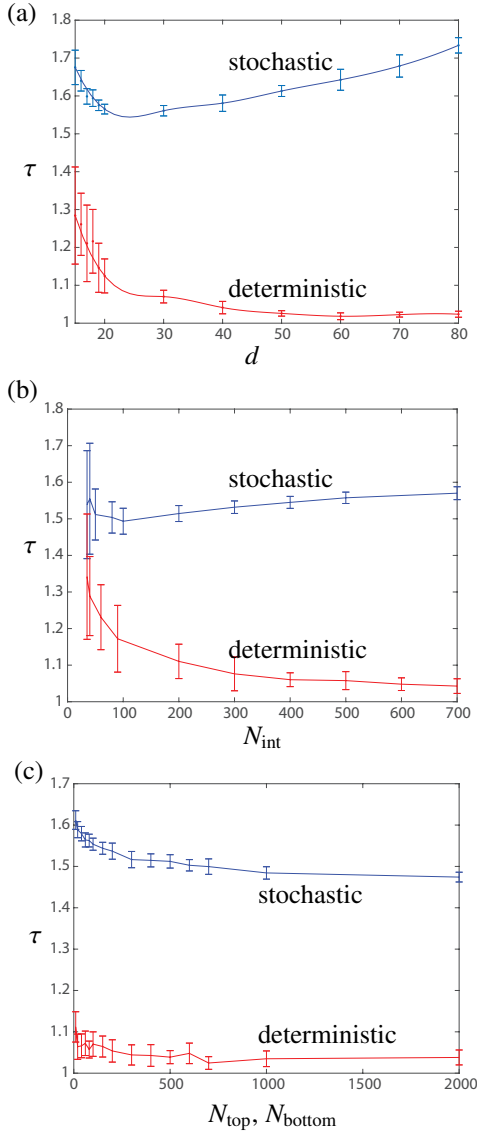
Figure 2: Tortuosity, τ versus (a) interconnectivity distance d, (b) number of internal pore junctions N_{int} and (c) the number of top or bottom pores, N_{top} or N_{bottom}. The blue curve shows the result for the stochastic model in which particles choose a probabilistic path that is biased by the flux through each pore at each junction. The red curve shows the result for a deterministic model in which the particles choose the path that corresponds to the highest flux, as given by equation (6). The tortuosity is determined by generating 30 different random filter configurations with the prescribed material parameters and calculating the tortuosity of the path taken by 200 different particles, choosing an initial pore location based on the flux for each filter configuration. The error bars show one standard deviation in the tortuosity measurements. In (a) we consider a filter with $N_{\text{int}} = 500$, $N_{\text{top}} = N_{\text{bottom}} = 100$; in (b) we choose $d = 30$, $N_{\text{top}} = N_{\text{bottom}} = 100$; and in (c) we choose $d = 30$ and $N_{\text{int}} = 500$ and either $N_{\text{top}} = 100$ or $N_{\text{bottom}} = 100$.

Although in this paper we shall use only the more realistic stochastic model, it is illuminating to consider the deterministic model to demonstrate show the effect that stochastic behaviour has on the fundamental system properties.

We observe a similar non-monotonic relationship between the tortuosity and the number of internal pore junctions, N_{int} (figure 2b, blue curve). Again this is attributed to the stochastic nature of the particle paths, which is confirmed by comparing with the deterministic model for which a monotonic relationship exists (figure 2b, red curve). While the tortuosity exhibits a non-monotonic relationship on interconnectivity distance and number of internal pore junctions, its relationship to the number of pores on either the top or bottom of the filter is monotonic (figure 2c). We note that the relationship is the same regardless of whether we choose to vary N_{top} or N_{bottom} as the initial tortuosity is independent of the orientation of the filter. For similar reasons, we find that the tortuosity is unaffected by the bias in pore location. We will find below, however, that the filter bias, introduced either by a mismatch in N_{top} and N_{bottom} or by a bias in the location of internal pore junctions will play a significant role in how the tortuosity varies with time as the filter blocks.

5. Relationship with physical properties

In practice one might envision being presented with a membrane in the form of tomographic data. From such data, one could extract the network properties by which we choose to define a membrane, namely through (1) and the parameters α, N_{int}, N_{top}, N_{bottom} and d (see, [15], for example).

However, a natural question to ask is, how can we relate our choice of filter characterization to other physical properties, such as the porosity distribution $\phi(z)$, the porosity gradient, $\mathrm{d}\phi/\mathrm{d}z$ and internal surface area of pores, S? In figure 3(a) we present the resulting porosity distribution, $\phi(z)$, for a given membrane characterization. As expected, the porosity gradient is approximately constant in the interior, and this gradient is linearly proportional to the parameter α in (1) (figure 3b). However, we are also able to capture the change in porosity near the top and bottom surfaces that results from our choice of characterization, through N_{top} and N_{bottom} (figure 3a).

The internal pore surface area, S, and porosity ϕ, both increase with interconnectivity distance, d, in a nonlinear way, with a power of approximately 3.9 in both cases (figure 4a,b). As a result, the parametric surface-area–

porosity plot achieved by varying the interconnectivity distance is approximately linear (figure 4c).

While a membrane may be characterized via a multitude of physical properties, the parameterization we choose here provides the clearest way to characterize a filter that possesses a porosity gradient and different surface porosities.
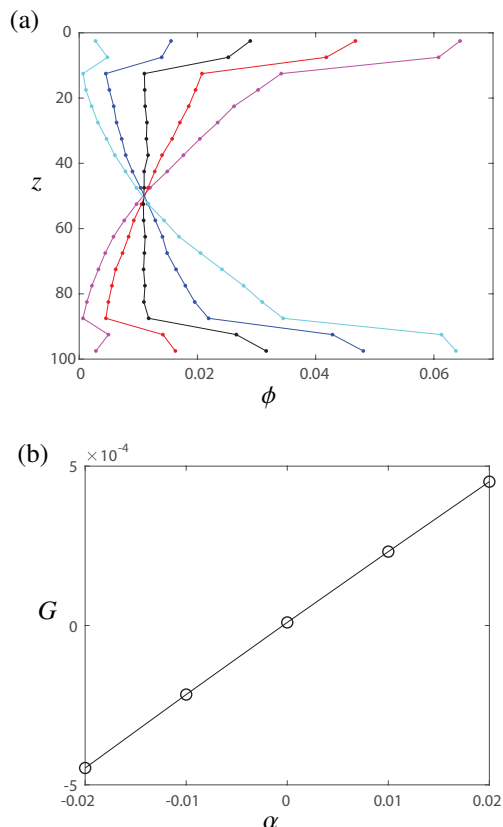
(a)

(b)

Figure 3: (a) Variation of porosity, ϕ, with filter depth, z, for a filter structure with a porosity gradient defined by (1). Here, $N_{int} = 500$, $N_{top} = N_{bottom} = 100$, $d = 21$, and $\alpha = -2/H, -1/H, 0, 1/H, 2/H$, with $H = 100$. (b) Relationship between internal porosity gradient, G, defined as the mean porosity gradient over the region $z \in [10, 90]$, and the parameter α in (1).

6. Influence of interconnectivity

We begin our assessment of the behaviour of the 3D filters by analysing their performance as we vary the filter properties. We first consider the interconnectivity, quantified through the interconnectivity distance d. We consider a filter with an unbiased porosity distribution ($\alpha = 0$, $N_{top} = N_{bottom} = 100$, $N_{int} = 500$) with particle size $a = 0.9$.
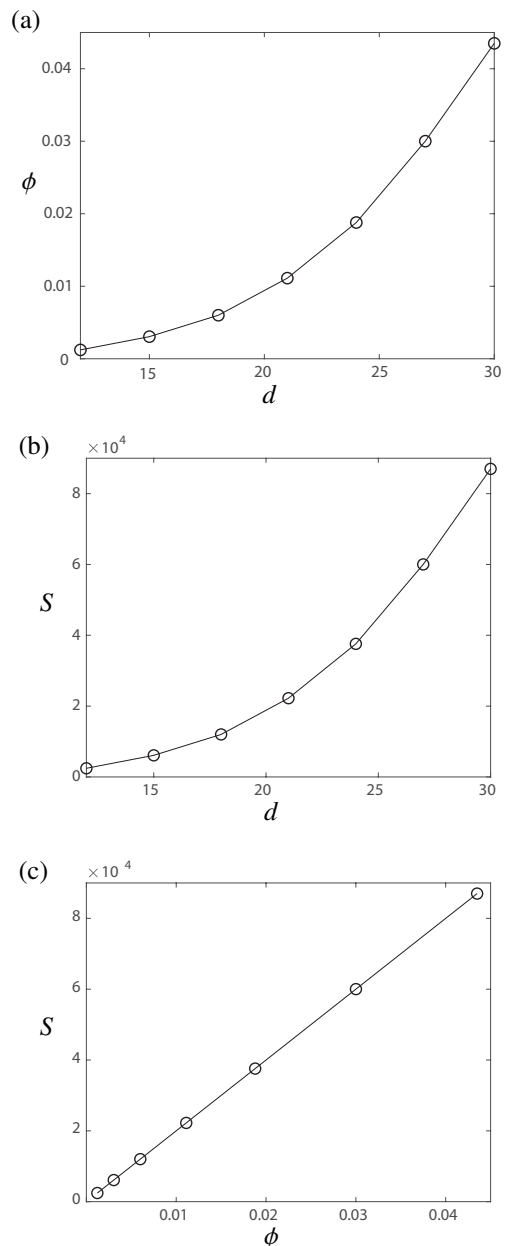
(a)

(b)

(c)

Figure 4: (a) Variation of mean porosity, ϕ, with interconnectivity distance, d, with $N_{int} = 500$, $N_{top} = N_{bottom} = 100$ and $\alpha = 0$. (b) Variation of internal pore surface area, S, with interconnectivity distance, d, with $N_{int} = 500$, $N_{top} = N_{bottom} = 100$ and $\alpha = 0$. (c) Parametric representation of the variation of internal pore surface area, S, with porosity, ϕ, achieved by varying interconnectivity distance, d, with $N_{int} = 500$, $N_{top} = N_{bottom} = 100$ and $\alpha = 0$. In all cases, we average over the internal domain $z \in [30, 70]$ to avoid the effect of the boundary layers observed in figure 3(a).

The flux–throughput graph is concave down (figure 5a), which is a result of the simultaneous internal
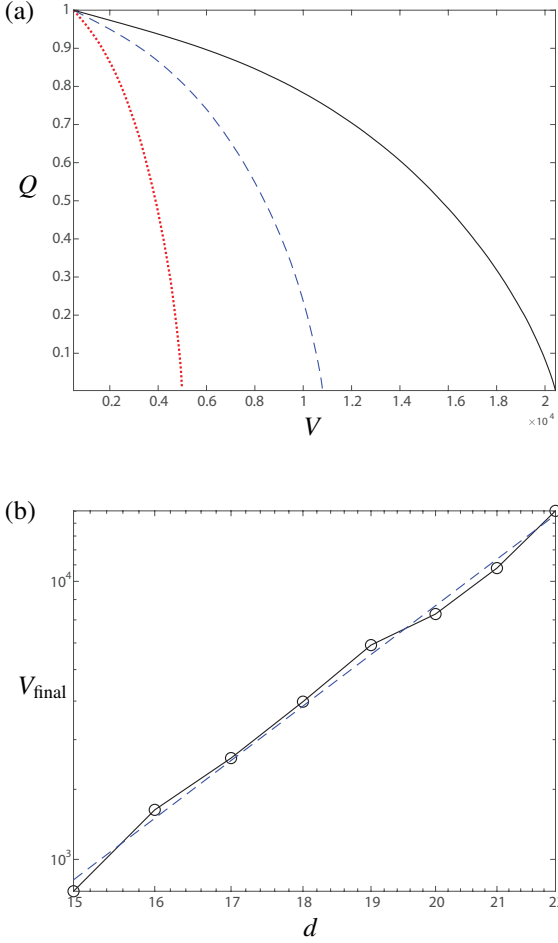
(a)

(b)

Figure 5: (a) Normalized flux, Q, versus throughput, V, for a filter with an unbiased pore distribution ($\alpha = 0$, $N_{\text{top}} = N_{\text{bottom}} = 100$ and $N_{\text{int}} = 500$) and interconnectivity distance $d = 18$ (red dotted), 21 (blue dashed) and 24 (black solid), with particle size $a=0.9$. When plotted versus the scaled throughput, V/V_{final}, the curves collapse onto a single master plot. (b) Log–log plot of final throughput, V_{final} versus interconnectivity, d. The blue dashed line shows the linear fit $\log_{10}(V_{\text{final}}) = 5.5 \log_{10}(d) - 3.2$.

fouling and complete blocking that takes place. This feature is discussed in more detail in [2] for a membrane comprising straight-through pores with no pore interconnectivity, as exhibited by track-etched membranes. The increase in the number of paths permissible through the filter offered by a higher interconnectivity expresses itself through a slower decline in the flux with throughput (figure 5a). The relationship between the final throughput at blocking, V_{final}, and interconnectivity distance, d, is seen to obey a power law, of the approximate form $V_{\text{final}} \propto d^{5.5}$ (figure 5b), though we acknowledge that this is only for the limited parameter range of d that we considered here. Plotting Q versus V/V_{final} we

find that the curves all collapse onto a single master plot (though we do not show this here). This indicates self-similarity of the system behaviour. This observation is especially noteworthy since it was found that for filters with regularly arranged pores the Q–V behaviour of a filter with no interconnectivity does not collapse onto the curves generated from a filter with interconnectivity between adjacent pores when scaled with final throughput [1]. This emphasizes the ability of the Q–V curve to expose properties in the underlying filter microstructure, as was found in [2].

As mentioned in the Introduction, this network model unlocks the potential to explore the way in which the tortuosity of paths taken by particles changes during the filtration process, and thus whether this property may be related to the overall filtration performance, and so we now turn our attention to this.

As the flux declines, we observe a concurrent rise in the tortuosity (figure 6a). This increase in tortuosity corresponds directly to an increase in the average distance a particle must travel before it passes out of the filter, as particles that have previously adhered to the pore walls obstruct the paths. The final tortuosity when the filter blocks completely also rises with increasing pore interconnectivity, but perhaps more interestingly, so does the initial tortuosity taken before fouling initiates. This indicates that, even in the absence of particle fouling, the randomness attributed to a particle path results in more convoluted paths being taken from the outset.

The increase in tortuosity will naturally lead to a greater chance of a particle being captured due to its increased exposure to the pore walls onto which it may adhere. This leads us to the natural question of how the particle removal efficiency, defined in (10), changes as the filtration process evolves. As anticipated, the removal efficiency of a filter will rise with throughput as a result of the increase in tortuosity (figure 6b).

Unlike the Q–V curves plotted in figure 5(a), neither the tortuosity nor removal efficiency curves in figures 6(a) or (b) collapse onto a single curve when scaled with the final throughput. However, when examining the relationship between removal efficiency and tortuosity we find this is independent of pore interconnectivity, with all curves lying on a single master curve (with variations among the curves lying within those expected due to stochastic variations) (figure 6c). Naively, one might expect this relationship between removal efficiency and tortuosity to be of the form of equation (7) with ℓ replaced with τ, that is

$$E = 1 - p_\tau = (1 - p_a)^\tau, \qquad (11)$$

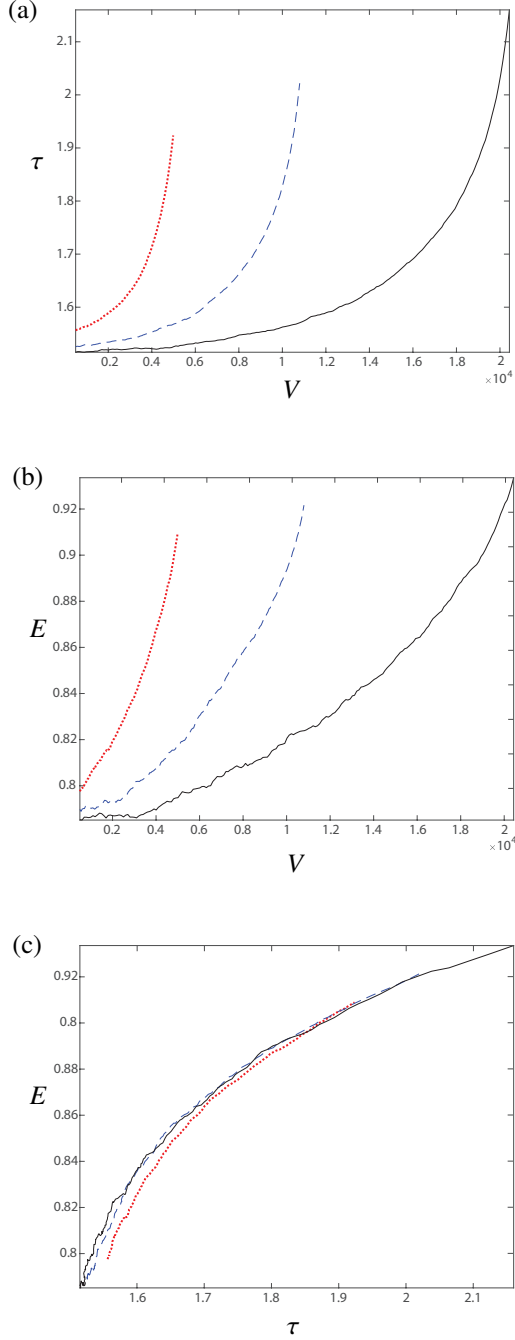since on average the particles are travelling a distance τ

Figure 6: Performance of a filter with an unbiased pore distribution ($\alpha = 0$, $N_{\text{top}} = N_{\text{bottom}} = 100$ and $N_{\text{int}} = 500$) and interconnectivity distance $d = 18$ (red dotted), 21 (blue dashed) and 24 (black solid), with particle size $a=0.9$. The performance is assessed by considering (a) Tortuosity, τ, versus throughput, V; (b) Particle removal efficiency, E, versus throughput, V; and (c) Particle removal efficiency, E, versus tortuosity, τ.

through the filter. However, this is not true. Since there is a spread of particle paths around this mean travel distance and the probability of adhering to the walls is a nonlinear function of travel distance, this skews the relationships so that the the mean particle removal efficiency is not simply related to the mean travel distance.

Thus, given the separation of behaviour when we plot the removal efficiency or tortuosity separately in terms of the throughput, and the nonlinear adhesion relationship, the collapse of this data is noteworthy and perhaps unexpected. This indicates that, regardless of whether the increase in interconnectivity is achieved through fabrication methods or as a result of paths being blocked by particle adhesion, the associated improvements in removal efficiency of a filter will be the same.

In practice, in a given filtration challenge one often wishes to maximize particle removal efficiency while also maintaining a large flux. Given the observed rise in efficiency and simultaneous fall in flux with throughput this provokes an optimization question of when a filter is performing at its 'best'. To attempt to answer this question, we consider the combined *performance metric*, M, defined as

$$M(V) = E(V) \cdot Q(V). \tag{12}$$

By studying figures 5(a) and 6(b) alone it is not immediately obvious how M will vary with throughput, and in particular whether it will be monotonic or possess an extremum during the filtration process. However, upon plotting this quantity, we discover that, in each case, M remains monotonically decreasing, indicating that the performance metric is always maximized initially (figure 7a). The performance metric is also seen to increase with increasing interconnectivity. Scaling M with its initial value and plotting versus V/V_{final} collapses all the curves onto a single master plot, in a similar manner to the Q–V curves. This demonstrates that the self-similarity in the filter interconnectivity is a property of both the Q–V relationship and the filtration efficiency metric.

Although the metric presented in (12) provides a mechanism for estimating the overall performance of the filter through a single parameter, one might imagine scenarios in which the particle removal efficiency is prized more highly than the flux. In this case, a generalized metric $M_\beta = E^\beta Q$ would be a more appropriate quantity of interest, where β measures the relative importance of removal efficiency to flux in the filtration challenge. The behaviour remains monotonic for order-one values for β, indicating that the performance is always best initially (figure 7b). When β is increased
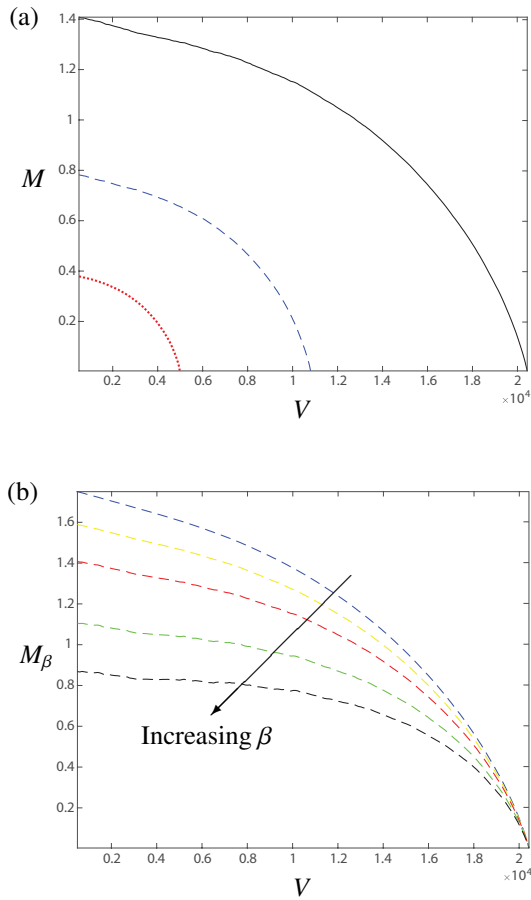
Figure 7: (a) The performance metric $M = EQ$ versus throughput V for a filter with interconnectivity distance $d = 18$ (red dotted), 21 (blue dashed), and 24 (black solid). When the performance metric scaled with its initial value is plotted versus the scaled throughput, V/V_{final}, each curve collapses onto a single master plot. (b) $M_\beta = E^\beta Q$ versus throughput V with $\beta = 0.1, 0.5, 1, 2, 3$ and $d = 24$. In both figures, we consider a filter with an unbiased pore distribution ($\alpha = 0$, $N_{\text{top}} = N_{\text{bottom}} = 100$ and $N_{\text{int}} = 500$), with particle size $a = 0.9$.

Figure 8: (a) Normalized flux, Q versus throughput V, for a filter with zero bias $\alpha = 0$ (red dotted), a bias towards the bottom $\alpha = 0.01$ (blue dashed) and a bias towards the top $\alpha = -0.01$ (black solid), with $N_{\text{top}} = N_{\text{bottom}} = 100$, $N_{\text{int}} = 500$, an interconnectivity distance $d = 18$ and particle size $a=0.9$. (b) Final throughput, V_{final} versus porosity gradient, α. When plotted versus the scaled throughput, V/V_{final}, each curve collapses onto a single master plot.

sufficiently, non-monotonic behaviour is eventually observed for $\beta \gtrsim 20$, corresponding to an optimal performance at an intermediate point in the filtration process. However, at this point the value of M is rather low and so the stochastic variations become important. (We do not show these curves here.) Large values of β correspond to prizing particle removal efficiency much more highly than flux, which would apply in situations where contaminant removal is vital, such as in virus removal.

7. Influence of porosity bias

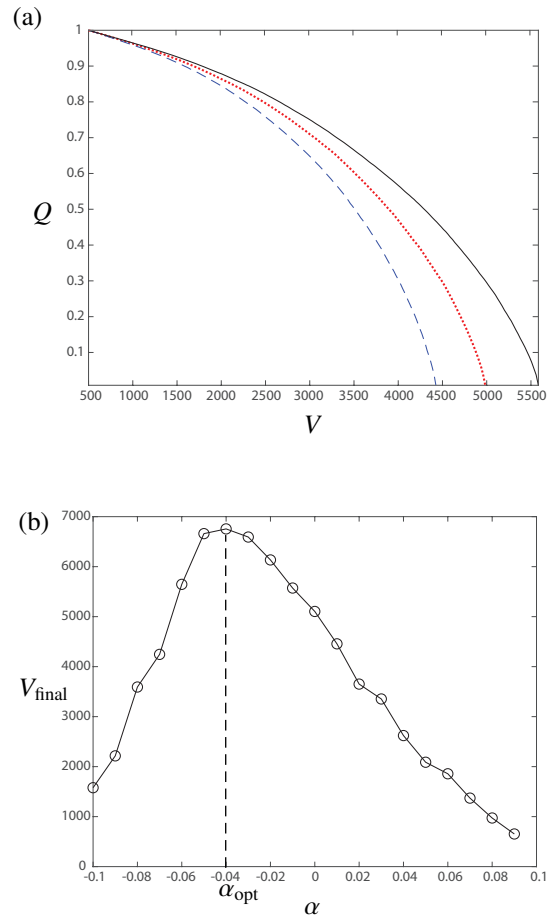We continue our assessment of filtration performance on the filter properties, now turning our attention to

study the influence of the porosity distribution. As discussed in the Introduction, a porosity bias can be implemented within our framework in two ways. The simplest way is by varying the porosity gradient in the internal structure, through the parameter α that appears in (1). This type of porosity gradient has been considered in [10, 11] in the context of filters comprising obstacles onto which contaminants adhere, which describes, for example, fibrous filters; our work here provides the porous-network analogue of this. The second route to obtaining a porosity gradient is by introducing a difference between N_{top} and N_{bottom}. This set-up may apply to composite filters that comprise membrane layers with

10

different porosities, which are used in gas separation, nanofiltration and reverse osmosis [12]. In this section we explore the influence of both types of porosity bias.

7.1. Internal porosity gradients

We begin by studying the effect of internal porosity gradients by varying the parameter α in the probability density function (1). In this case, the Q–V curves in figure 8(a) show that the flux decline is minimized for filters where more pores are placed towards the top of the filter. This is in accord with the observations made for fibrous filters [10, 11]. In a similar manner to the Q–V curves obtained when varying interconnectivity, we also observe self-similarity when we plot the Q–V curves with respect to the scaled throughput V/V_{final}.

In figure 8(b) we plot the variation of final throughput with respect to how strongly biased the filter is, represented through the porosity gradient α. We find that a higher throughput is achieved by filters with more pores distributed towards the top portion of the filter interior. The reason for this observation is that pores located further into the depth of the filter will see fewer particles as many will have already been removed by the upper pores. Allowing for a greater number of pores in the upper part of the filter will lead to a more uniform distribution of particles in the pores when the filter finally blocks. However, continuing to increase the bias in the porosity towards the top of the filter will lead to insufficient pores in the lower layer to accept the arriving particles and the filter will block sooner. This gives rise to a non-monotonic dependence of throughput on α. A similar observation was made for a non-woven filter medium [10, 11]. We find an optimal porosity gradient described by $\alpha = \alpha_{\mathrm{opt}} \approx -0.04$ in (1).

The tortuosity at any given throughput increases with increasing bias towards the top of the filter, as well as the maximum (final) tortuosity that can be attained (figure 9a). Likewise, the particle removal efficiency improves as the pores are biased towards the top (figure 9b).

As in the case where we varied the interconnectivity distance, we find that, although both the tortuosity and removal efficiency vary with bias, variations in the bias are not expressed through the relationship between removal efficiency and tortuosity (figure 9c).

The initial removal efficiency of each filter is seen to be unaffected by the bias (recall that the initial removal efficiency varies with interconnectivity distance, as seen in figure 7a). This shows that the removal efficiency depends on the mean porosity of the filter (which we hold constant in each case by definition of our porosity function (1)) (figure 9c). The superior performance of a fil-
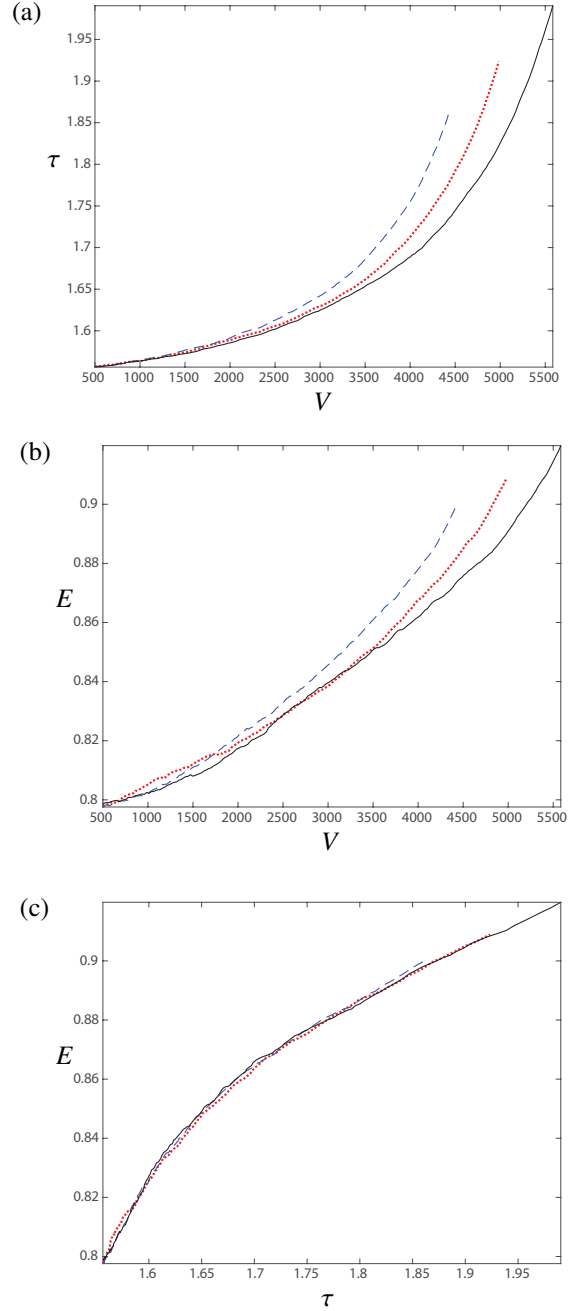

(a)

(b)

(c)

Figure 9: Performance of a filter with zero bias $\alpha = 0$ (red dotted), a bias towards the bottom $\alpha = 0.01$ (blue dashed) and a bias towards the top $\alpha = -0.01$ (black solid), with $N_{\mathrm{top}} = N_{\mathrm{bottom}} = 100$, $N_{\mathrm{int}} = 500$, an interconnectivity distance $d = 18$ and particle size $a=0.9$. The performance is assessed by considering (a) Tortuosity, τ, versus throughput, V; (b) Particle removal efficiency, E, versus throughput, V; and (c) Particle removal efficiency, E, versus tortuosity, τ.
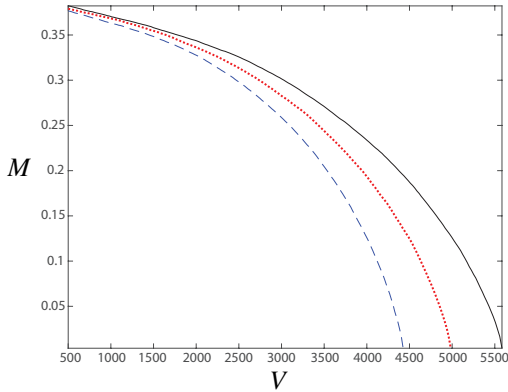
Figure 10: The performance metric $M = EQ$ versus throughput V for a filter with zero bias $\alpha = 0$ (red dotted), a bias towards the bottom $\alpha = 0.01$ (blue dashed) and a bias towards the top $\alpha = -0.01$ (black solid), with $N_{\text{top}} = N_{\text{bottom}} = 100$ and $N_{\text{int}} = 500$, an interconnectivity distance $d = 18$, and particle size $a = 0.9$. When plotted versus the scaled throughput, V/V_{final}, each curve collapses onto a single master plot.

ter whose pores are biased towards the top is, however, evident as time progresses (figure 10). When the performance metric M is plotted versus scaled throughput, V/V_{final}, all curves collapse onto a single master plot.

7.2. Top and bottom porosity differences

We now turn our attention to achieving a bias in the porosity by considering a difference between the top and bottom surface porosities, N_{top} and N_{bottom}. The surface layers mimic composite filters that are composed of a thin 'skin' layer and an underlying porous support structure [12].

We study the effect of varying the top surface porosity relative to the bottom surface porosity while we hold the mean porosity constant (*i.e.*, $N_{\text{top}} + N_{\text{bottom}}$ is held fixed). In this case, we find that the Q–V curves are largely insensitive to differences in $N_{\text{top}} - N_{\text{bottom}}$ over a wide range (indicated by the plateau in figure 11b). Thus, unlike in the case of an internal bias, there is not a clear optimum porosity difference between the top and bottom surfaces. If this difference is increased by a suitable amount either in the positive or negative sense then the throughput eventually falls as a result of either too few top surface pores or too few bottom surface pores (figure 11a). Plotting the flux versus the scaled throughput V/V_{final} again leads to a collapse to a master plot.

When considering the evolution of the tortuosity we find similarly that the behaviour is the same over a broad range of values for $N_{\text{top}} - N_{\text{bottom}}$. If $N_{\text{top}} - N_{\text{bottom}}$ is too negative, so that the number of pores on the top is too

low, then the tortuosity starts off lower than that when N_{top} and N_{bottom} are similar to each other, but eventually crosses over at some point, and takes larger values thereafter. When $N_{\text{top}} - N_{\text{bottom}}$ is large and positive, so that the number of pores on the bottom is too low, the tortuosity is always lower than that when N_{top} and N_{bottom} are similar to each other (figure 12a). A similar behaviour is observed for the removal efficiency (figure 12b). As in previous examples, the removal efficiency versus tortuosity curves are all approximately the same, though a small distinction can now be made (figure 12c).

The curves for performance metric M are improved to begin with when $N_{\text{top}} - N_{\text{bottom}}$ is either large and positive or large and negative but cross over at some point with the curve for the case when N_{top} and N_{bottom} are similar (figure 13).
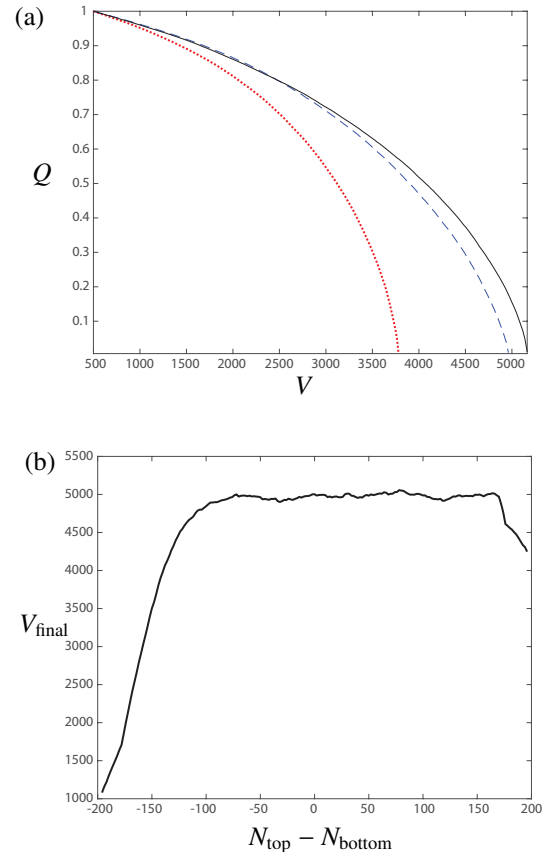
(a)

(b)

Figure 11: (a) Normalized flux, Q versus throughput V, a filter with a bias towards the bottom $N_{\text{top}} - N_{\text{bottom}} = -150$ (red dotted), zero bias $N_{\text{top}} - N_{\text{bottom}} = 0$ (blue dashed) and bias towards the top $N_{\text{top}} - N_{\text{bottom}} = 180$ (black solid) while $(N_{\text{top}} + N_{\text{bottom}})/2 = 100$, with $\alpha = 0$, $N_{\text{int}} = 500$, an interconnectivity distance $d = 18$ and particle size $a = 0.9$. (b) Final throughput, V_{final}, versus $N_{\text{top}} - N_{\text{bottom}}$.
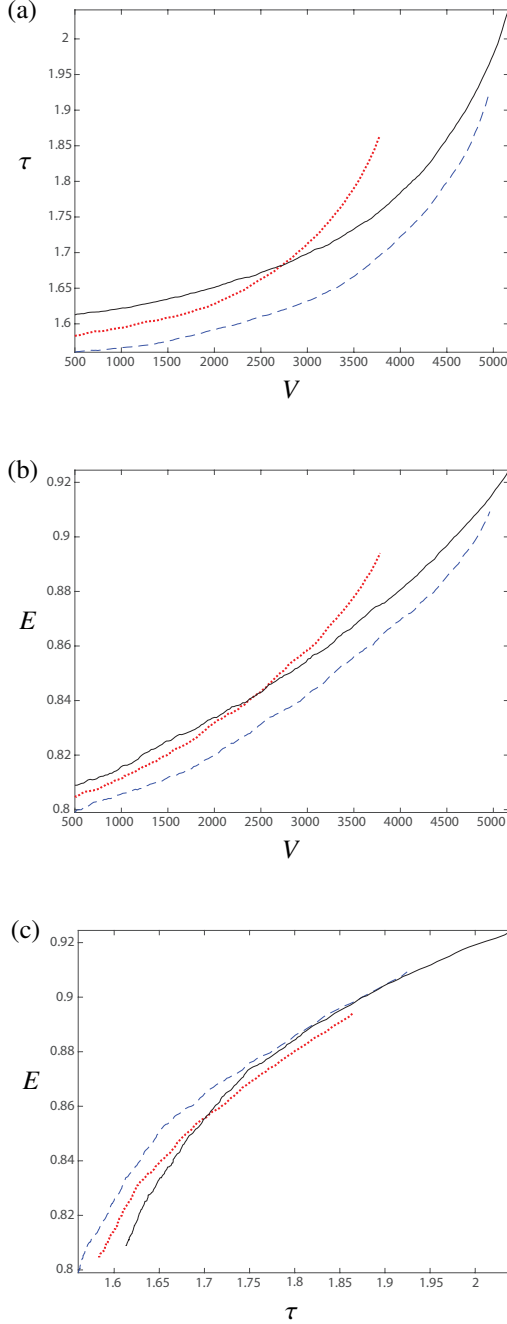
(a)

(b)

(c)

Figure 12: Performance of a filter with a bias towards the bottom, $N_{\text{top}} - N_{\text{bottom}} = -150$ (red dotted), zero bias, $N_{\text{top}} - N_{\text{bottom}} = 0$ (blue dashed) and bias towards the top $N_{\text{top}} - N_{\text{bottom}} = 180$ (black solid) with $(N_{\text{top}} + N_{\text{bottom}})/2 = 100$, $\alpha = 0$, $N_{\text{int}} = 500$, an interconnectivity distance $d = 18$ and particle size $a=0.9$. The performance is assessed by considering (a) Tortuosity, τ, versus throughput, V; (b) Particle removal efficiency, E, versus throughput, V; and (c) Particle removal efficiency, E, versus tortuosity, τ.
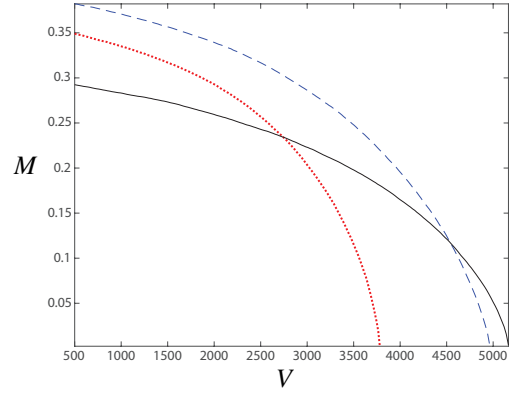

Figure 13: The performance metric $M = EQ$ versus throughput V for a bias towards the bottom, $N_{\text{top}} - N_{\text{bottom}} = -150$ (red dotted), zero bias, $N_{\text{top}} - N_{\text{bottom}} = 0$ (blue dashed) and bias towards the top $N_{\text{top}} - N_{\text{bottom}} = 180$ (black solid) with $(N_{\text{top}} + N_{\text{bottom}})/2 = 100$, $\alpha = 0$, $N_{\text{int}} = 500$, an interconnectivity distance $d = 18$ and , with $\alpha = 0$, an interconnectivity distance $d = 18$, and particle size $a = 0.9$.

8. Influence of particle size

Having assessed the performance of a given filter given its physical properties we conclude by exploring the filter performance when subjected to different feeds, by varying the size of the particles being filtered. We use a filter with no porosity bias ($\alpha = 0$ in (1)), and set $N_{\text{top}} = N_{\text{bottom}} = 100$, $N_{\text{int}} = 500$ and an interconnectivity distance $d = 18$. We restrict our attention to monodisperse feeds and vary the particle size, $a < 1$ so that particles are able to enter the pores and internal fouling occurs. As noted in §2.3, when $a > 1$ all particles are sieved at the surface of the filter, which is not of interest here. We keep the probability of adhering to the pore wall, $p_a = 0.01$ in all cases.

As the particle size increases the blocking process is accelerated, as expected (figure 14a). A feature that has been present in all of the analysis conducted so far is that when the filter properties were adjusted the Q–V curves exhibited self-similarity when plotted versus the scaled throughput V/V_{final}. Performing the same process for the curves in figure 14(a) however no longer leads to a collapse onto a single master plot. Thus the self-similarity that was present when material properties of the filter were varied does not extend to variations in the feed. We attribute this to different blocking mechanisms at play: larger particles lead to pores blocking completely more quickly, so that a greater proportion of pores are no longer accessible sooner.

The tortuosity and particle removal efficiency both rise more sharply with increasing particle size (fig-
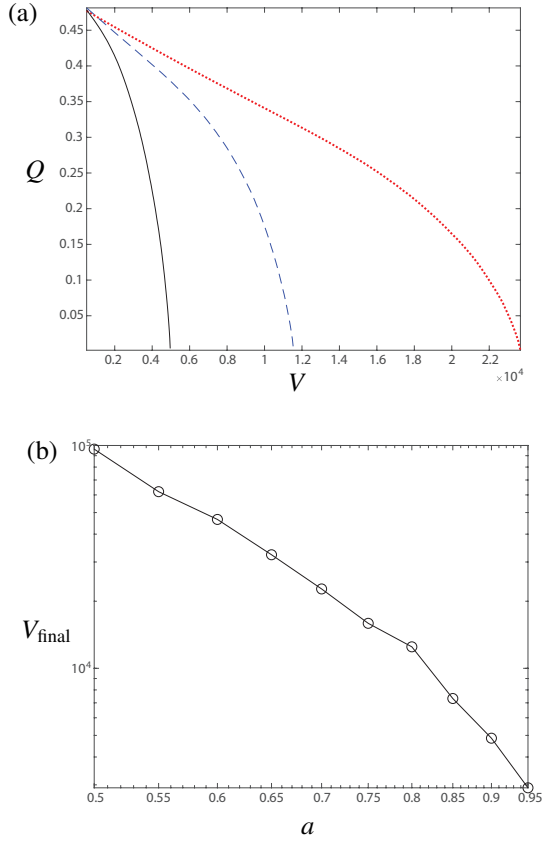
13

Figure 14: (a) Normalized flux, Q versus throughput V, an unbiased pore distribution ($\alpha = 0$, $N_{\text{top}} = N_{\text{bottom}} = 100$ and $N_{\text{int}} = 500$) and interconnectivity distance $d = 18$, with particle size $a=0.7$ (red dotted), $a=0.8$ (blue dashed) and $a=0.9$ (black solid). (b) Final throughput, V_{final} versus particle size, a.
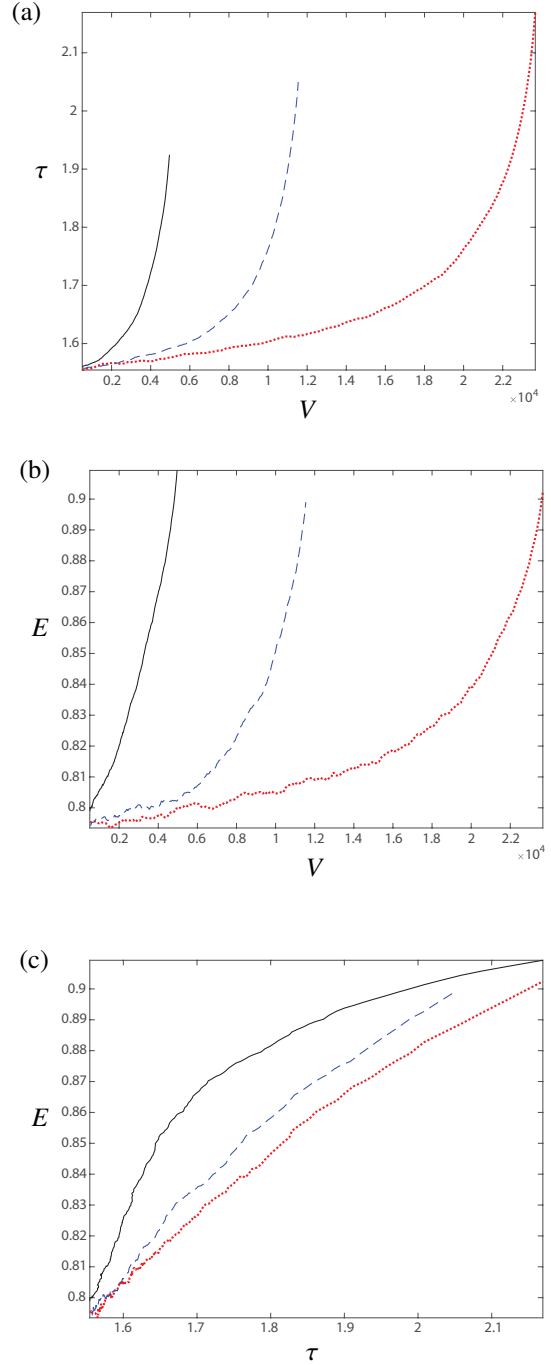

Figure 15: Performance of a filter with an unbiased pore distribution ($\alpha = 0$, $N_{\text{top}} = N_{\text{bottom}} = 100$ and $N_{\text{int}} = 500$) and interconnectivity distance $d = 18$, with particle size $a=0.7$ (red dotted), $a=0.8$ (blue dashed) and $a=0.9$ (black solid). The performance is assessed by considering (a) Tortuosity, τ, versus throughput, V; (b) Particle removal efficiency, E, versus throughput, V; and (c) Particle removal efficiency, E, versus tortuosity, τ.

ure 15a,b). The relationship between removal efficiency and tortuosity exposes a dependence on particle size (figure 15c). This is in contrast to the results obtained for variations in the material properties of the filter, which did not present themselves in the relationship between removal efficiency and tortuosity.

The performance metric M reduces with increasing particle size (figure 16). In a similar manner to the Q–V curves, the dependence of the performance metric on scaled throughput, V/V_{final} also does not reduce to a single master curve, unlike all previous studies for variations in material properties of the filter.

9. Conclusions

We have presented a fully general framework to describe the evolution in the performance of a filter during the filtration process. The framework models fil-
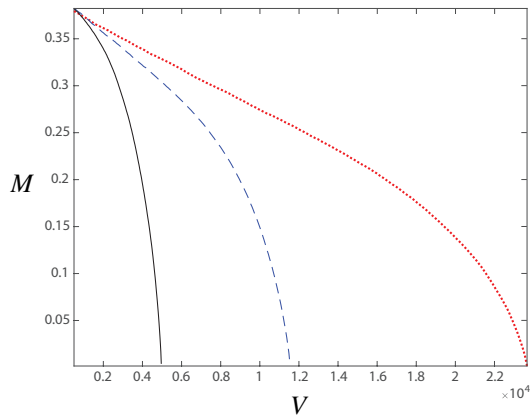
14

Figure 16: (a) The performance metric $M = EQ$ versus throughput V for a filter with an unbiased pore distribution ($\alpha = 0$, $N_{\text{top}} = N_{\text{bottom}} = 100$ and $N_{\text{int}} = 500$), interconnectivity distance $d = 18$, and particle size a=0.7 (red dotted), a=0.8 (blue dashed) and a=0.9 (black solid).

ter structures comprising a fully random network of interconnected pores, the more traditional simplifying assumptions on periodicity in the filter geometry that enable a model to be more tractable.

The network model outlined here provides a fully generalized version of the simpler frameworks outlined in [1, 2], and makes a step towards encapsulating the full complexity of a filter within a framework that is easy to implement and study. The model allowed us to perform a comprehensive study of the performance of a filter on both the filter structure (expressed through the pore interconnectivity and porosity gradient) and the feed composition (expressed through the size of the contaminants).

The flexibility in the model allowed us to extract simple scaling laws from this complex underpinning network structure. In particular, we found that a universal self-similarity was expressed in the flux–throughput curves upon variations in the filter structure when scaled with the final throughput. In contrast, when we turned our attention to studying the impact of variations in the feed properties, which we explored by varying the particle size, we found that this self-similarity was no longer present. In particular, the flux–throughput curves no longer collapsed onto a single master curve.

The most notable advantage of this model is its ability to link the notion of tortuosity to a filter's performance. In doing so we were able to uncover further self-similarity, in the relationship between particle removal efficiency and tortuosity, a result that was not easily anticipated by studying the evolution of these properties during filtration. We found that the removal-efficiency–

tortuosity relationship was unaffected by changes in the material property of the filter, but did exhibit a dependence on the particle size in the feed.

Our network model allows us to probe the behaviour of a complex and realistic filter configuration in a simple and tractable manner. We expect that the model can be used in real-life scenarios, to enable accelerated testing of various filter challenges, as well as reduce the number of costly experiments that are traditionally required to ensure that a filtration unit is operating in the desired manner.

Acknowledgements

[1] I. M. Griffiths, A. Kumar, P. S. Stewart, Designing asymmetric multilayered membrane filters with improved performance, J. Membr. Sci. 511 (2016) 108–118.

[2] I. M. Griffiths, A. Kumar, P. S. Stewart, A combined network model for membrane fouling, J. Colloid and Interf. Sci. 432 (2014) 10–18.

[3] P. Sanaei, L. J. Cummings, Membrane filtration with complex branching pore morphology, Phys. Rev. Fluids 3 (2018) 094305.

[4] G. Printsypar, M. Bruna, I. M. Griffiths, The influence of porous media microstructure on filtration, J. Fluid Mech. 861 (2019) 484–516.

[5] A. J. Burggraaf, K. Keizer, Synthesis of inorganic membranes, in: Inorganic Membranes Synthesis, Characteristics and Applications, Springer, 1991, pp. 10–63.

[6] S. Barg, D. Koch, G. Grathwohl, Processing and properties of graded ceramic filters, Journal of the American Ceramic Society 92 (2009) 2854–2860.

[7] L. E. Anderson, Filter element and method of making the same, 1951. US Patent 2,539,768.

[8] I. Vida-Simitfi, N. Jumate, V. Moldovan, G. Thalmaier, N. Sechel, Characterization of gradual porous ceramic structures obtained by powder sedimentation, J. Mat. Sci. & Technol. 28 (2012) 362–366.

[9] D. Dickerson, M. Monnin, G. Rickle, M. Borer, J. Stuart, Y. Velu, W. Haberkamp, J. Graber, Gradient density depth filtration system, 2006. US Patent App. 11/140,801.

[10] M. P. Dalwadi, M. Bruna, I. M. Griffiths, A multiscale method to calculate filter blockage, Journal of Fluid Mechanics 809 (2016) 264–289.

[11] M. P. Dalwadi, I. M. Griffiths, M. Bruna, Understanding how porosity gradients can make a better filter using homogenization theory, Proc. R. Soc. A 471 (2015) 20150464.

[12] R. J. Petersen, Composite reverse osmosis and nanofiltration membranes, J. Membrane Sci. 83 (1993) 81–150.

[13] H. Ockendon, J. R. Ockendon, Viscous Flow, Cambridge University Press, 1995.

[14] J. Bear, Dynamics of fluids in porous media. Elsevier, New York (1972).

[15] J. Jimenez-Martinez, C. F. A. Negre, Eigenvector centrality for geometric and topological characterization of porous media, Phys. Rev. E 96 (2017) 013310.